FULL PAPER

Experiment to distinguish two fumaroles consistently emanating infrasound at Kirishima Iwo-Yama

Kazuya Yamakawa[1]* , Mie Ichihara[2], Dan Muramatsu[2], Takeshi Matsushima[3], Hidetoshi Takahashi[4], Ruka Wada[4] and Isao Shimoyama[5]

Abstract

In the infrasonic observation of a fumarolic field, distinguishing multiple fumarolic sources is challenging. The array technique effectively estimates the source locations and identifies the target signal from other signals and noise. We conducted an experiment at Kirishima Iwo-Yama, Japan, where two active fumarolic areas were separated by ~ 450 m. A three-element array with an aperture of ~ 20 m was installed between the two fumarolic areas. In addition, a single microphone was installed near one of the fumaroles. The array combined with the waveform correlation analysis estimated the most prominent source but failed to estimate the other weak source. A joint analysis of the array and the single microphone effectively resolved the two sources. It was also confirmed that newly developed power-saving MEMS microphones were useful for observing the fumaroles. This paper presents the instrumentation and analytical method that would be beneficial for monitoring volcanoes that have multiple hydrothermally active vents.

Keywords Infrasound, Volcano, Fumarole, Array observation

Graphical Abstract
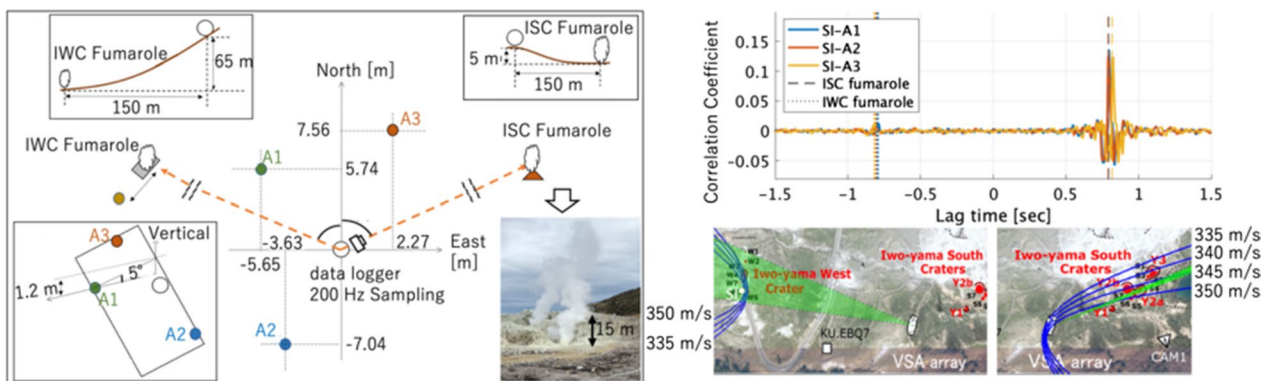
*Correspondence:
Kazuya Yamakawa
yamakawa@mfri.pref.yamanashi.jp
Full list of author information is available at the end of the article

Yamakawa *et al. Earth, Planets and Space*   (2023) 75:26

Page 2 of 12

Introduction

Distinguishing multiple acoustic sources is a challenge during infrasonic monitoring of volcanoes having multiple active vents. In Stromboli, Italy, several vents are active simultaneously (e.g., Chouet et al. 1997; Ripepe and Marchetti 2002; Salvatore et al. 2018; Yamakawa et al. 2022). In some volcanoes, flank eruptions formed multiple new vents emanating infrasound, like the 2006 and 2007 eruptions of Etna, Italy (Marchetti et al. 2009; Cannata et al. 2009) and the 2007 eruption of Kilauea, Hawaii (Fee et al. 2011). Also, multiple new vents can open in phreatic eruptions, like the 2018 eruption of Kirishima Iwo-Yama, Japan (Muramatsu et al. 2021). Historically, Sakurajima has erupted simultaneously at the eastern and western flanks in 1914 (Iguchi 2013). In many cases, infrasound analysts avoid the multiple source problem by choosing the time windows or assuming that the most significant single source produces most of the observed waveform (e.g., Ripepe and Marchetti 2002; Yokoo et al. 2014; Yamakawa et al. 2022). These methods are effective when a transient large-amplitude signal, such as an explosion wave, is observed or a single crater's activity is more significant than that of others. However, the multiple sources matter when no signal is dominant because all of their amplitudes are similar among them or are as low as the noise.

A fumarole is a vent that emanates steam and other volatiles, such as carbon dioxide and sulfur dioxide, in an active volcanic environment (McKee et al. 2017). Its geochemical signatures provide information about subsurface volcanic activity (Wallace 2005; Fischer 2008). Because fumaroles can be active even when the volcano is not eruptive, they can be good observation targets in field experiments. Some studies have focused on the acoustic noise emanating from a fumarole (Woulff and McGetchin 1976; McKee et al. 2017). McKee et al. (2017) investigated infrasound associated with the gas-jetting from the Naka-dake crater of Aso Volcano (Japan). They found low-amplitude sustained broadband (0.5–25 Hz) infrasonic signals and compared their power spectra with laboratory jet noise spectra (Tam et al. 2008) to estimate the jet velocity. Eventually, they converted the jet velocity to a total volatile flux. Their work suggested a new monitoring method for fumaroles.

Active hydrothermal fields often host multiple fumaroles within several hundred meters. For example, La Fossa Crater, Vulcano Island, Italy, has countless vents in the 0.045-km^2 fumarolic field (Aiuppa et al. 2005), and Kirishima Iwo-Yama, Kyushu, Japan, has six or more fumaroles within a 0.01-km^2 area (Tajima et al. 2020, see also Fig. 1b). Because the fumarolic infrasound is weak, it is often obscured by wind noise and needs a high-performance recording microphone for detection. A very-small-aperture (VSA) array having an aperture a few tens of meters wide (Yamakawa et al. 2018, 2022) may contribute to resolving such signals. To assess the applicability of our instrumentation in multiple-vent fumarole fields, we conducted an experiment using a VSA array at Kirishima Iwo-Yama. This paper presents the results and discusses the performance and improvements we made to VSA array observation to resolve multiple sources.

Kirishima Iwo-Yama

The experiment was conducted on 19–20 October 2020 at Kirishima Iwo-Yama (hereafter just Iwo-Yama), Kyushu, Japan (Fig. 1), where several active fumaroles existed. The detail of the Iwo-Yama's activity was documented by Tajima et al. (2020) and is shortly summarized below. Since December 2015, the fumarolic activity had been varying with the changes in the thermal anomaly area where the temperature (measured by a thermocouple at ∼10 cm deep) was higher than 50 °C. The fumaroles' formation and jetting with audible sound around the Iwo-Yama summit crater started in 2017. On 19 April 2018, the phreatic eruption occurred at the Iwo-Yama south crater (ISC) and then the Iwo-Yama west crater (IWC) became active. Muramatsu et al. (2021, 2022) reported the infrasonic activities of the ISC and IWC during the phreatic eruption in April 2018. They identified two simultaneous sources using data recorded at two infrasound stations: a prominent source from the ISC and a weaker one from the IWC (Fig. 1b). Muramatsu et al. (2022) documented the detail of the infrasonic activity at the ISC in the eruption period comparing with the images by a monitoring camera.

During our observation period (18–19 October 2020), the Y2a and Y3 vents in the ISC and the W4 vent in the IWC (Fig. 1b; Tajima et al. 2020; Muramatsu et al. 2021)

(See figure on next page.)

Fig. 1 Kirishima Iwo-Yama and the observation array. **a** The locations of Kirishima Iwo-Yama and nearby regional meteorological stations. **b** The locations of the craters (ISC and IWC), vents (Y1–T3, W3, W4), the SI microphone, and the VSA array, modified from Fig. 3 of Tajima et al. (2020). **c** An overview of the field experiment. **c1** The observation geometry consisting of the VSA array (microphones A1–A3) and the SI microphone with respect to the ISC and IWC fumaroles. **c2**, **c3** The topographic features between the VSA array site (white circle) and the IWC fumarole (**c2**), and the ISC fumarole (**c3**). **c4** The ground dip at the array site. **d** An image of the ISC fumarole taken from the array location (the camera symbol shown in c1)
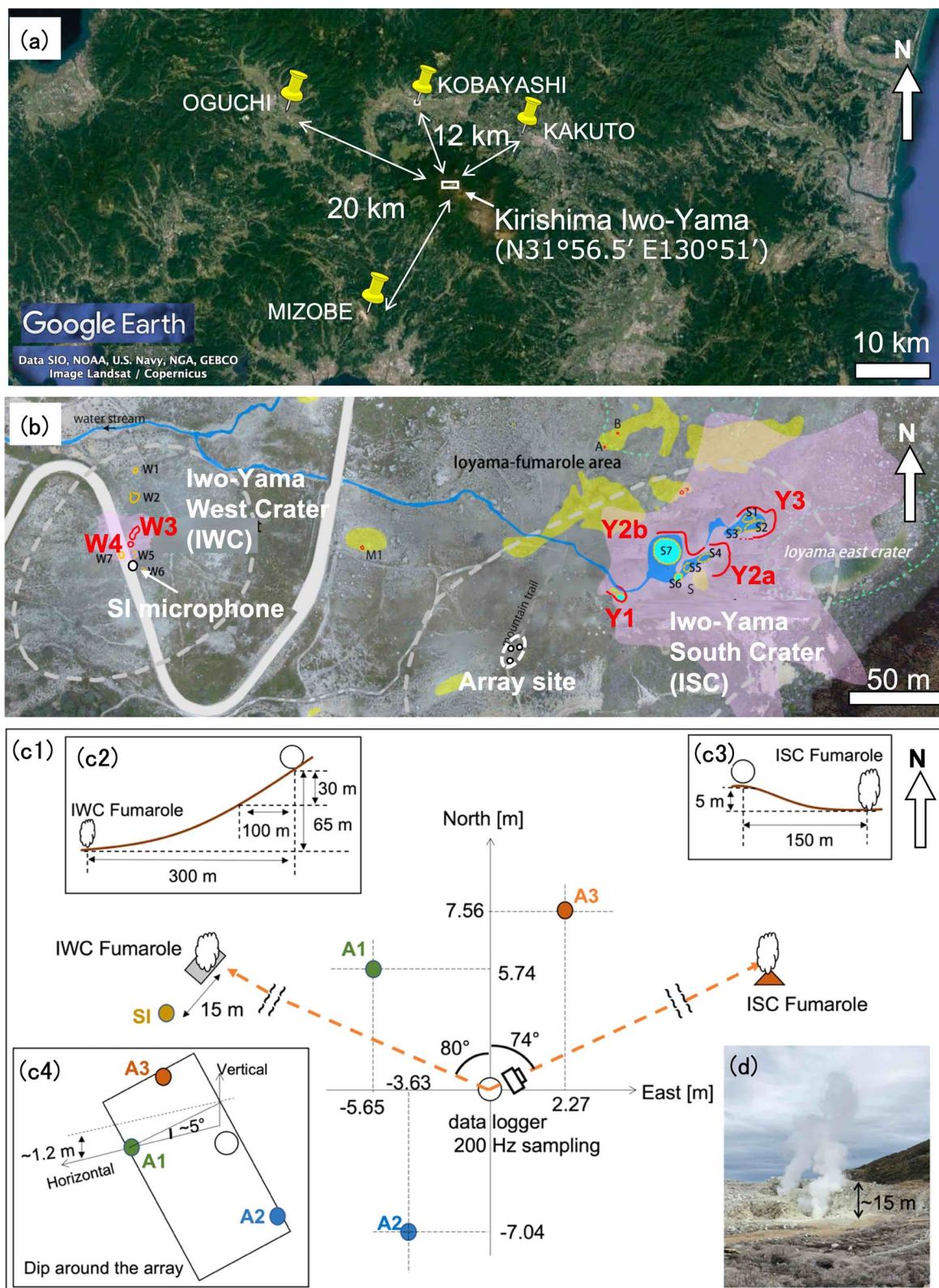
Fig. 1 (See legend on previous page.)

Yamakawa *et al. Earth, Planets and Space*   (2023) 75:26

Page 4 of 12

were both still persistently steaming (Fig. 1d), but their activity was much weaker than the one reported by Muramatsu et al. (2021, 2022). The acoustic signals from the calm activity of multiple fumaroles of Iwo-Yama had not been observed and analyzed in detail. The main purpose of this paper is to resolve the infrasonic signals from these two craters. Hereafter, we refer to the Y2a and Y3 vents as the ISC fumarole and the W4 vent as the IWC fumarole (Fig. 1b).

Observations

A three-element VSA array with an aperture of 15 m was installed between the ISC and IWC fumaroles (Fig. 1c). The distances from the array to the ISC and IWC fumaroles were 150 m and 300 m, respectively. The array was operated from 17:30 on 18 October 2020 to 12:30 on the next day (Japan Standard Time). We inferred that the temperature and wind at Iwo-Yama during the operation were 6–14 °C and 0–3 m/s, respectively, as reported by the regional meteorological stations (Fig. 1a) (Additional file 1: S1).

Each element of the VSA array was a condenser microphone (Type7744N, ACO Co., flat response in 0.1–1000 Hz, power consumption ~ 3 mA, self-noise ~ 0.0009 Pa, sensitivity ~ 8 mV/Pa), hereafter referred to as ACO microphones (A1, A2, and A3). The VSA array with microphones of this type successfully estimated the back azimuths with the error of ~ 2 and ~ 5 degrees in > 5 Hz and 1–5 Hz, respectively, even though it had significant errors below 1 Hz due to its small aperture (Yamakawa et al. 2022). We placed each ACO microphone in a small box to protect it from rain. A 3-channel 24-bit data logger (LS8800, HAKUSAN Co.) recorded the data at 200 Hz with an anti-aliasing filter (a low-pass filter below 80 Hz).

Because phreatic eruption jets and fumarolic jets generally produce weak infrasound (McKee et al. 2017; Muramatsu et al. 2021, 2022), we anticipated that the signals at Iwo-Yama were subtle, even below the microphones' self-noise. Therefore, we enclosed a newly developed high-sensitivity microelectromechanical systems (MEMS) microphone (Wada and Takahashi 2020; Additional file 1: S2) together with each ACO microphone, expecting that the use of two different types of microphones could confirm the robustness of the results. We put the documentation about the MEMS microphones in Supporting Information (Additional file 1: S2 and S3) because the waveforms and results are essentially identical to those with the ACO microphones (Fig. 2a).

In addition to the array, a single microphone (SI102, HAKUSAN Co., flat response in 0.1–1500 Hz, power consumption of < 25 mA, self-noise ~ 0.02 Pa, sensitivity ~ 1 mV/Pa) was installed near the IWC fumarole.

Hereafter, we refer to it as the SI microphone. The distances from the SI microphone to the IWC and ISC fumaroles were ~ 15 m and ~ 450 m, respectively. The SI microphone was housed in a box with a data logger (HKS-9700, KGC Co.). The data were recorded at 1000 Hz in 24 bit from 11:30 to 12:30 on 20 October 2020, when the temperature and wind speed at Iwo-Yama were inferred to be ~ 12 °C and ~ 3 m/s, respectively (Additional file 1: S1).

Analysis

Because the fumarole continuously emanated infrasound, the waveforms had no apparent onset. The waveforms recorded by the array microphones had dominant frequencies at ~ 10 and ~ 35 Hz, though such spectral peaks were not obvious in the SI microphone's record (Fig. 2d; see also Additional file 1: S4). The waveform correlation between the array elements was retained good up to 80 Hz (the upper limit band of the 200 Hz sampling with the anti-aliasing instrumental filter) during the observation period (Additional file 1: S4). In contrast, low-frequency components below 5 Hz depended significantly on time, affected by wind noise (see the "Results" section). From above, we decided to use the bands above 5 Hz. Because we did not know the frequency contents of all signals, we used the broad band (5–80 Hz) in the analyses.

We calculated the cross-correlation functions (CCFs) and cross-correlation coefficients (CCs). To improve the signal-to-noise ratio, we stacked the CCFs and CCs for each microphone pair in successive time windows. Each CCFs and CC was calculated using a 1-min time window. Note that different window lengths produced the same results due to the persistency of the signals. Sixty successive CCFs and CCs for time windows overlapping by 59 s (namely, the 2-min-long data) were stacked. Hereafter, the term "CCF" and "CC" indicates the stacked ones.

The SI microphone might have recorded a significant signal from the IWC fumarole because it was located in close proximity (only ~ 15 m away, Fig. 1c). Therefore, the cross-correlations (CCs and CCFs) between the SI and array microphones were also analyzed. Hereafter, we call the CC between the SI microphone and each element of the array the "SI-array CC" and distinguish it from the CC between a pair of the array elements (denoted as the "array CC"). We stacked the SI-array CCs with intervals longer than 30 min to resolve the weak signal and applied the lag time fitting method to the SI-array CCs.

As the array analysis, we applied the grid search method (Johnson and Palma 2015; Yamakawa et al. 2018). We defined the lag time as the arrival time difference between a sensor pair. We modeled the lag times as functions of the slowness vector, assuming the plane
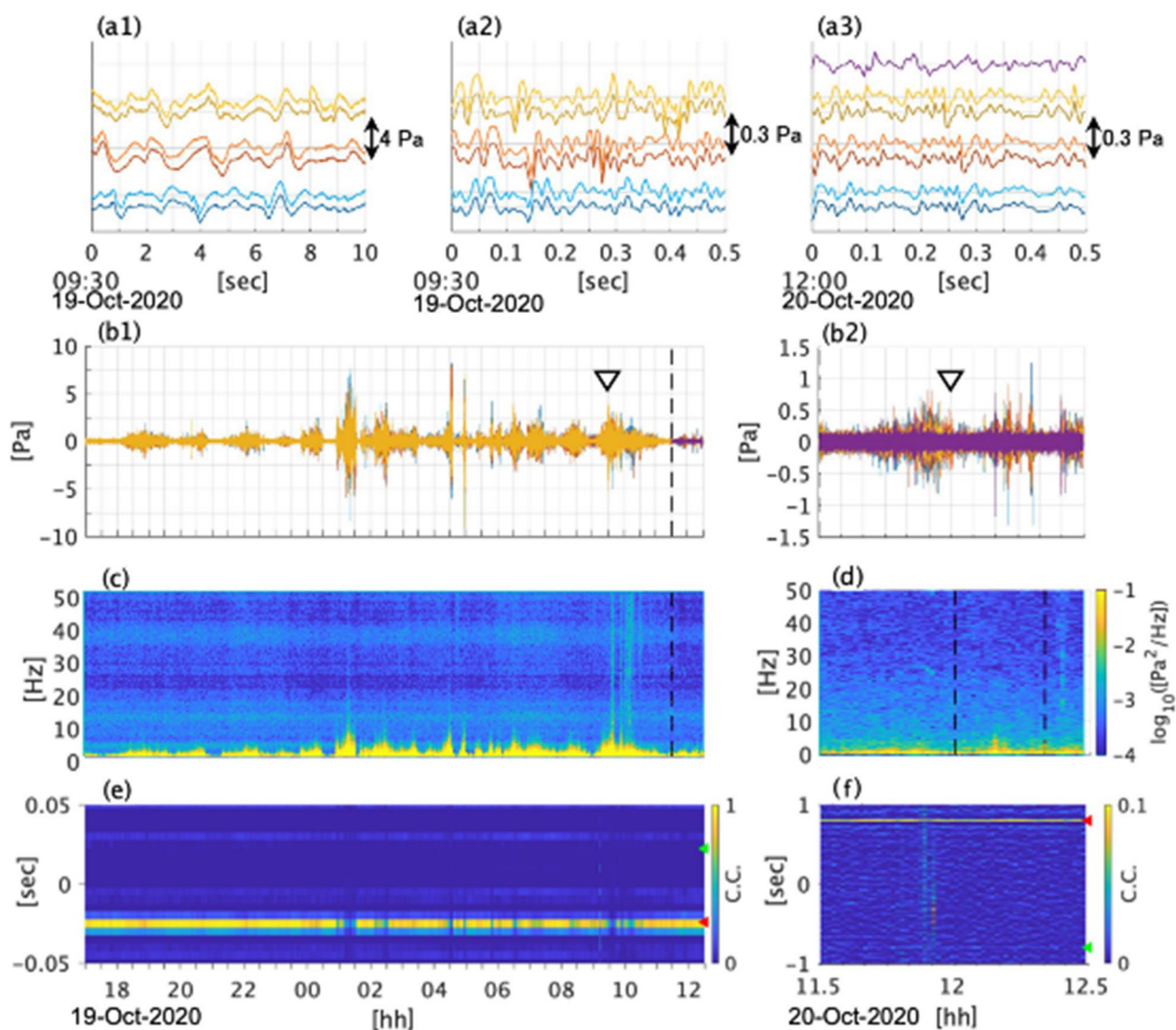
Fig. 2 Waveforms, spectrograms, and correlation coefficients. **a** Examples of the observed waveforms at 0.3–80 Hz (**a1**, **a3**) and 5–80 Hz (**a2**). The line colors indicate the microphones (blue, A1; red, A2; yellow, A3; purple, SI). The lower darker blue, red, and yellow lines in (**a1**–**a3**) show the waveforms recorded by the collocated MEMS microphones. **b–f** The waveforms at 0.3–80 Hz (**b1**, **b2**), the spectrograms (**c**, **d**), and the cross-correlation coefficients (CCs) (**e**, **f**) acquired during the array observation on the left (**b1**, **c**, **e**) and with the SI observation on the right (**b2**, **d**, **f**). The black dashed line in **b1** indicates the start time for **b2**. The black triangles in **b1** and **b2** mark the origin times of **a1**, **a2** and **a3**, respectively. The displayed spectrograms are of A1 (**c**) and SI (**d**), the array CC between A1 and A3 (**f**), and the SI-array CC between SI and A1 (**e**) using the waveforms at 5–80 Hz. The arrowheads on the right axis in **e** and **f** indicate the lag times between the microphones assuming the ISC source (red) and IWC source (green). The waveforms, spectrograms, and CCs for the other microphones are presented in Additional file 1: S4

wave propagation. Then, we calculated the lag times on the slowness grids of the northward and eastward components from −6.0 to 6.0 s/km with the 0.01 s/km interval. On the other hand, we estimated the observed lag time by maximizing the stacked correlation for each sensor pair. Finally, we searched for the slowness grid that gave the smallest fitting residual (the mean square of the differences between the observed and modeled lag times of all the sensor pairs).

Results

Figure 2b–f presents some examples of the waveforms, spectrograms, and CCs obtained from our analysis. Other data are shown in Additional file 1: S4. Although the enlarged waveforms of the individual array elements are sometimes different (Fig. 2a), the spectral structures of A1–A3 are consistent in time and similar to each other (Additional file 1: Fig. S4.1). The power below 5 Hz is significantly time-dependent (Fig. 2c). When the

Yamakawa *et al. Earth, Planets and Space* (2023) 75:26

Page 6 of 12

low-frequency power is large, the array CCs become poor (Additional file 1: Fig. S4.2). We infer that the temporally varying low-frequency components are due to wind noise because the correlation in the whole bands becomes smaller when the low-frequency power is larger (Additional file 1: Fig. S4.2). When the wind speed is v, wind noise with a frequency f loses correlation beyond a distance of $v/(3f)$ (Shields 2005). At a distance of 10 m, wind noise above 0.3 Hz should have little correlation under normal wind speeds.

In contrast, the higher components above 5 Hz are stable (Fig. 2c) and coherent among the array elements (Fig. 2e), indicating the existence of a persistent infrasound signal. The signal firstly arrives at A3, secondly at A1 ~ 0.025 s after A3, and finally at A2 with a slight delay after A1. These lag times clearly indicated that the signal propagates from an eastern source, i.e., the ISC fumarole, at the acoustic speed (Fig. 3a, see also Additional file 1: Fig. S5a).

The SI microphone data exhibit waveforms and spectral structures different from those of the array microphones even above 5 Hz (Fig. 2a3, d). We infer that the SI microphone might have recorded signals from different sources, which we discuss later in more detail for the SI-array CCs. Here, we focus mainly on the persistent signal above 5 Hz, using data acquired during the operation of all microphones (from 11:30 to 12:30 on 20 October).

The lag times obtained from the array CCs suggest an acoustic signal from the ISC direction. However, there are no apparent correlation peaks indicating the IWC fumarole (Fig. 3a). The MUSIC algorithm (Schmidt 1986) and the CLEAN beamforming (den Ouden et al. 2020) also failed to resolve the IWC fumarole's source (Additional file 1: S5), at least with the current three-element array. The reason of this failure is discussed later ("Power ratio of the two sources" section).
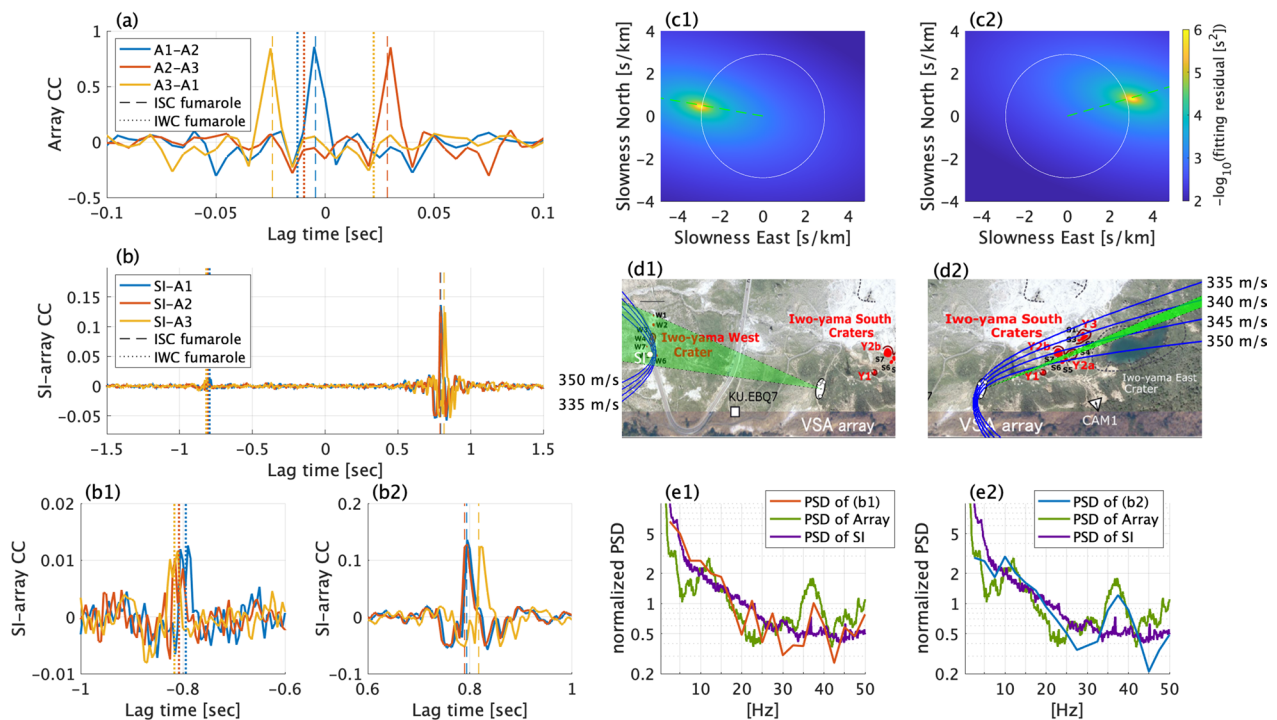

Fig. 3 Correlation coefficients (CCs) and the array analysis results. **a** The array CC and **b** SI-array CC at 5–80 Hz. Enlarged view of **b** around the minor peak (**b1**) and the prominent peak (**b2**). The vertical lines with the corresponding colors mark the calculated infrasound propagation time differences between the microphone pairs, assuming that the sources are located at the IWC fumarole (dotted lines) and the ISC fumarole (dashed lines). The lag time fitting results for the peaks in **b1** and **b2** are shown in **c1**, **d1** and **c2**, **d2**, respectively. **c** The fitting residual using all pairs of SI-array CC is shown as functions of horizontal components of the slowness. The white circles indicate acoustic slowness. **d** The blue curves indicate the source hyperbola obtained from the SI–A1 lag time fitting assuming the propagation velocities as 335, 340, 345, and 350 m/s. The green angle range from the VSA array shows the estimated back azimuth (2 STD) obtained from **c**. The white and red points mark the microphones' and fumaroles' locations, respectively. **e** The power spectra densities (PSDs) normalized by the power in the main bands ranging from 5 to 50 Hz, which were calculated using the three CCs in **b1** and **b2** are shown in **e1** by the red line and in **e2** by the blue line, respectively. They are compared with the PSD for the array microphones (green) and the PSD for the SI microphone (purple). For the former (the green line), the normalized PSDs for the individual array microphones are averaged

However, each SI-array CCs shows a prominent peak for a positive lag time and unclear small peaks for a negative lag time (Fig. 3b). By stacking the CCs for longer than 30 min, the small peaks become a single peak for each of the SI-array CCs (Fig. 3b1, Additional file 1: S6). The lag times of these minor peaks are consistent with the signal from the direction of the IWC fumarole (Fig. 3c1), while the prominent peak (Fig. 3b2) corresponds to the direction of the ISC fumarole (Fig. 3c2). It should be noted that ambient noise can also form a pair of peaks, with a symmetrically to zero time delay, in the cross-correlation between two stations. The peaks represent Green's function between the station pair (Shapiro and Campillo 2004; Ortiz et al. 2021). However, it is more probable that the observed correlation peaks are comprised of fumarolic signals rather than ambient noise (discussed in "Correlation response" section). The result indicates that the SI-array CC analysis successfully identified the contribution of the IWC fumarole with a time resolution of $\sim$ 30 min.

Even if there are only two microphones (SI and one of the array elements, e.g., A1), the lag time for each peak of the single SI-array CC can constrain the source hyperbola. We draw the hyperbola assuming the acoustic velocities of 335–350 m/s, corresponding to the temperatures of 6–23 °C (blue lines in Fig. 3d). Both fumarolic areas are near the hyperbolas. Combining the hyperbola and the back-azimuth obtained by all the SI-array CCs (Fig. 3c) well constrained the source area (Fig. 3d).

Based on Parseval's theorem, the power spectrum can be derived from the cross-correlation functions (CCFs). Because the SI-array CC resolved the contribution of each source, the Fourier transform of the SI-array CCF in a limited lag-time range around each peak should give the power spectral density (PSD) for the corresponding source signal. Thus, we obtained the PSDs for the ISC fumarole signal (Fig. 3e1) and the IWC fumarole signal (Fig. 3e2).

Discussion

Power ratio of the two sources

Some array analysis methods, such as MUSIC (Schmidt 1986) and CLEAN beamforming (den Ouden et al. 2020), are designed to resolve multiple sources. However, these methods with the current dataset identify only the ISC fumarole signals (Additional file 1: Fig. S5). Namely, the analyses fail to distinguish the ISC and IWC fumaroles simultaneously. This failure may relate to the significantly larger power of the ISC fumarole signal compared to the IWC's.

We estimated the individual source power, assuming simple monopole sources (e.g., Woulff and McGetchin 1976). The monopole source amplitudes can be calculated from their associated source-receiver distances and the peak values of the cross-correlation functions. We modeled the waveforms $F^a(t)$ at the array and $F^b(t)$ at the SI microphone as follows:

$$F^a(t) = \frac{S_1\left(t - \tau_1^a\right)}{\left|\boldsymbol{y}_1 - \boldsymbol{x}^a\right|} + \frac{S_2\left(t - \tau_2^a\right)}{\left|\boldsymbol{y}_2 - \boldsymbol{x}^a\right|} + N^a(t), \qquad (1)$$

$$F^b(t) = \frac{S_1\left(t - \tau_1^b\right)}{\left|\boldsymbol{y}_1 - \boldsymbol{x}^b\right|} + \frac{S_2\left(t - \tau_2^b\right)}{\left|\boldsymbol{y}_2 - \boldsymbol{x}^b\right|} + N^b(t), \qquad (2)$$

where $\boldsymbol{x}^n$ and $N^n(t)$ indicate the location and noise at the station n (a or b), respectively; $S_m(t)$ and $\boldsymbol{y}_m$ indicate the source time function and location of the source m (1 or 2), respectively; and τ_m^n indicates the travel time from source m to station n. For the convenience, we define $\Delta\tau_m = \tau_m^b - \tau_m^a$ and $\Delta\tau^n = \tau_2^n - \tau_1^n$. We assume that the correlations between the two sources, source and noise, and noise at the two stations are negligible, namely, $E[S_1(t)S_2(t)] = E[S_m(t)N^n(t)] = E\left[N^a(t)N^b(t)\right] = 0$, where $E[\cdot]$ is the ensemble average. In addition, because $\Delta\tau_1$ and $\Delta\tau_2$ are significantly different (the locations of the colored dotted lines and colored dashed lines in Fig. 4b, respectively), the correlation between $S_m(t - \Delta\tau_1)$ and $S_m(t - \Delta\tau_2)$ is assumed to be negligible compared to the power of the sources, namely, $E[S_1(t)S_1(t)] \gg E[S_2(t - \Delta\tau_1)S_2(t - \Delta\tau_2)]$ and $E[S_2(t)S_2(t)] \gg E[S_1(t - \Delta\tau_1)S_1(t - \Delta\tau_2)]$. Considering the general relation $E[f_1(t)f_2(t + T)] = E[f_1(t - T)f_2(t)]$ for arbitrary functions f_1 and f_2, we obtain the relation that $E[S_m(t - \Delta\tau_1)S_m(t - \Delta\tau_2)] = E\left[S_m(t - \Delta\tau^a)S_m\left(t - \Delta\tau^b\right)\right]$. Then, we can calculate the power of the sources PS_1 and PS_2 as follows:

$$PS_m = E[S_m(t)S_m(t)] \simeq \left|\boldsymbol{y}_m - \boldsymbol{x}^a\right|\left|\boldsymbol{y}_m - \boldsymbol{x}^b\right|$$
$$E\left[F^a\left(t + \tau_m^a\right)F^b\left(t + \tau_m^b\right)\right], \qquad (3)$$

where $E\left[F^a\left(t + \tau_m^a\right)F^b\left(t + \tau_m^b\right)\right]$ may be evaluated from the peak values for the SI-array CCFs. Once PS_1 and PS_2 are obtained, we can calculate the noise power at the n-th station PN^n as follows:

$$PN^n = E\left[F^n(t)F^n(t)\right] - \frac{PS_1}{\left|\boldsymbol{y}_1 - \boldsymbol{x}^n\right|^2} - \frac{PS_2}{\left|\boldsymbol{y}_2 - \boldsymbol{x}^n\right|^2}. \qquad (4)$$

Note that this monopole assumption holds several problems. Firstly, the laboratory jet noise exhibits complex radiation patterns and correlation behaviors (Tam et al. 2008). Secondly, the volcanic jet could be
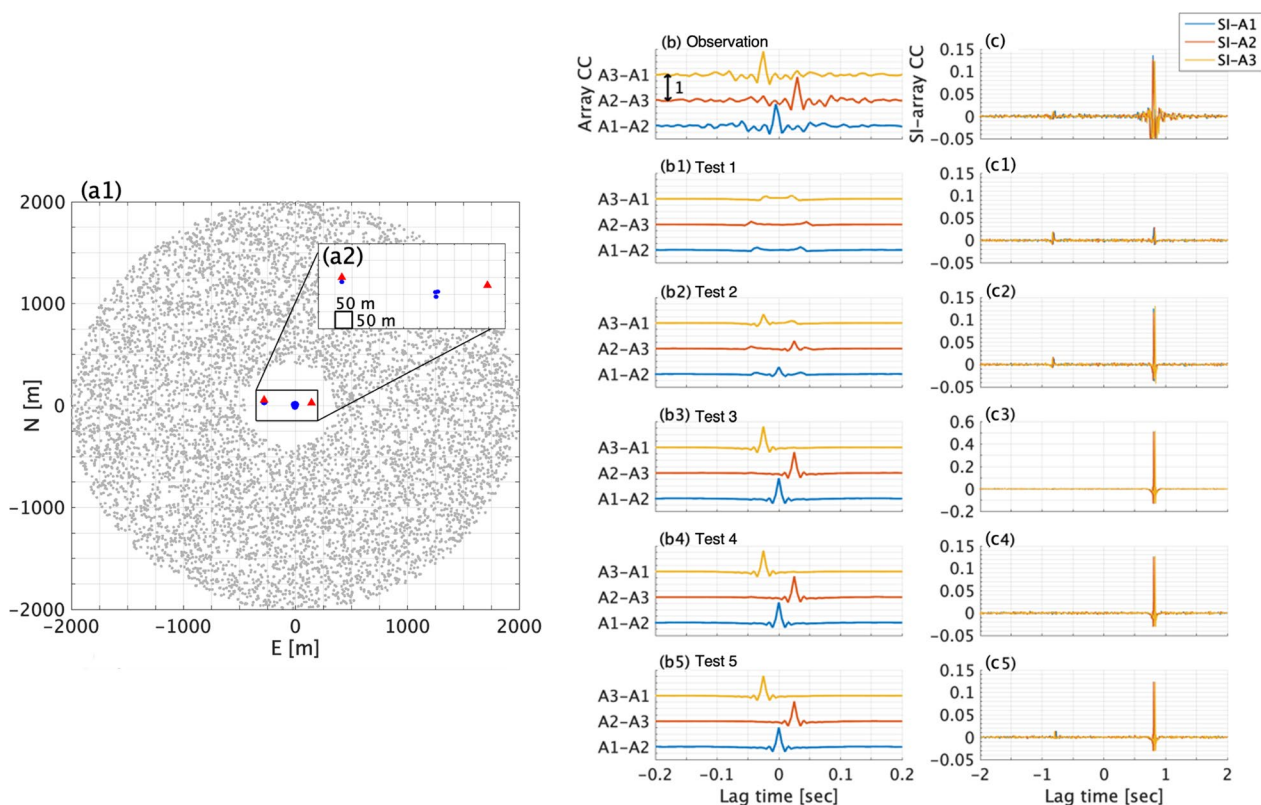
Fig. 4 The correlation peaks generated by ambient noise (correlation responses). **a1** The locations of the microphones (blue points), signal sources (red triangles), and ambient noise sources (gray dots). **a2** An enlarged view of **a1**. **b**, **c** The observed array CCs (**b**) and SI-array CCs (**c**). They are compared with the synthetic array CCs (**b1–b5**; the vertical scales are identical to that of **b**) and SI-array CCs (**c1–c5**). The numbers 1–5 indicate the synthetic test numbers in Table 2

a multi-pole infrasound source, mainly consisting of a monopole and a dipole (Iezzi et al. 2022). Nevertheless, we regard that this approach provides the approximate estimation of the two fumarolic source powers because the monopole radiation is the most efficient.

The results are shown in Table 1. The source amplitude of the ISC fumarole is estimated to be larger than that of

the IWC fumarole by one or two orders of magnitude. Although the SI microphone is near the IWC fumarole (~15 m distant), the ISC fumarole's power is comparable to that for the IWC fumarole. This emphasizes that it is crucial to identify the multiple sources, even when we place a microphone very close to a target source. It is also noted that the estimated signal levels are as small

Table 1 Summary of the infrasound sources

	ISC fumarole	IWC fumarole	Noise
Distance from the array (m)	150	300	–
Distance from the SI microphone (m)	450	15	–
Peak value of the array CC	0.80	–	–
Peak value of the SI-array CC	0.13	0.01	–
Monopole source amplitude (at 1 m) (Pa)	3	0.2	–
RMS amplitude at the array (Pa)	0.0200	0.0007	0.0223
RMS amplitude at the SI microphone (Pa)	0.0067	0.0140	0.0257
Power fractions at the array (%)	44.4	0.1	55.5
Power fractions at the SI microphone (%)	5.0	21.8	73.2

as 0.0007 Pa at the ACO microphones and 0.0067 Pa at the SI microphone (Table 1), which are smaller than the nominal self-noise levels for the microphones, as provided by the manufacturers (ACO: 0.0009 Pa; SI:0.02 Pa). The cross-correlation analyses help identify such small signals by suppressing the noise. We obtained essentially same results using the waveforms recorded by MEMS microphones, which supported the robustness of the results.

Correlation response

The cross-correlation of a random isotropic wavefield recorded at two stations can represent the Green function between the stations (Shapiro and Campillo 2004; Bensen et al. 2007; Wapenaar et al 2011), which helps to estimate the seismic velocity structures and their temporal variations (e.g., Brenguier et al. 2008; Tonegawa et al. 2009; Hirose et al. 2017; Nishida et al. 2020). Although the atmosphere is a time-dependent moving medium, such seismic processing has been successfully applied in the infrasound studies (Haney et al. 2009; Ortiz et al. 2021). However, the emergence of the Green function is problematic in the current analysis. The numerical test assuming enormous ambient noise sources around the stations (Fig. 4a) shows that the synthetic array CC and SI-array CC (explained later) exhibit a pair of peaks (Fig. 4b1, c1, respectively). In this study, we call such ambient-noise-related peaks in the CCs the "correlation response."

What matters is that the CCs can exhibit two minor but significant peaks without any infrasound signals due to the correlation response (Fig. 4c1). Because the IWC peak in the SI-array CC is small (Fig. 3b1), it is not easy to distinguish whether it represents the correlation response or the IWC fumarole signal. In the former case, there should be another minor peak around $+0.8$ s in the SI-array CC because the correlation response should emerge symmetrically with respect to the zero-lag time (Fig. 4b1, c1). However, the correlation peak for the ISC fumarole signal may mask such a peak (Fig. 3b2). In addition, because the SI microphone was near the IWC fumarole, it was not easy to distinguish the IWC fumarolic signal and the correlation response from the SI microphone with the array analysis (Fig. 3d1).

Here, we describe synthetic tests to investigate the correlation response. All the stations and fumaroles were approximated on a single plane for simplicity (Fig. 4a). We also assumed the ambient noise sources in the same plane because they are confirmed to make more distinct correlation responses than those out of the plane. The waveform, $F^n(t)$, recorded at the n-th microphone at $\boldsymbol{x}^n$, consists of two dominant signals (i.e., two fumarolic

sources), local non-acoustic noise, and random acoustic noise from the numerous weak acoustic sources:

$$
\begin{aligned}
F^n(t) = \ & A_1 \frac{s_1\left(t - \tau_1^n\right)}{\left|\boldsymbol{y}_1 - \boldsymbol{x}^n\right|} + A_2 \frac{s_2\left(t - \tau_2^n\right)}{\left|\boldsymbol{y}_2 - \boldsymbol{x}^n\right|} \\
& + A_{\text{noise}}^n s_{\text{noise}}^n(t) + \sum_k A_k \frac{s_k\left(t - \tau_k^n\right)}{\left|\boldsymbol{y}_k - \boldsymbol{x}^n\right|},
\end{aligned}
\tag{5}
$$

where s_1 and s_2 are the normalized synthetic waveforms from the ISC and IWC fumaroles, respectively; s_{noise}^n is the non-acoustic noise at the n-th microphone, uncorrelated between the microphones; and s_k is the normalized acoustic noise from the k-th ambient source. Their amplitudes are denoted by A_1, A_2, A_{noise}^n, and A_k, respectively. The source-to-station propagation times of the acoustic waves are τ_1^n, τ_2^n, and τ_k^n, and the source locations are $\boldsymbol{y}_1$, $\boldsymbol{y}_2$, and $\boldsymbol{y}_k$, respectively. We distributed 10,000 ambient sources in 4×4 km^2 area and then picked the sources within 2 km of the stations except for the nearest 400 m of the mid-point (Fig. 4a) to avoid ambient sources having a power larger than that of the fumarolic signals. As a result, 7000–8000 ambient sources were used. Note that the minor difference of the ambient source distribution did not affect the results. Gaussian noise filtered at 5–80 Hz was used as the synthetic source waveforms. All the synthetic source waveforms (s_1, s_2, s_{noise}^1, s_{noise}^2, and each of noise waveforms s_k) are independent each other and thus all the cross-correlations between the source waveforms are negligible. The synthetic CCs were calculated in 1-min time windows with 60 min stacking.

We calculated the synthetic array-CCs (Figs. 4b1–b5) and SI-array CCs (4c1–c5) for several conditions (Table 2) and compared them with the observations (Fig. 4b, c). The results are summarized in Table 2. As expected, the synthetic CCs without fumarolic signals show small symmetric peaks in the correlation response (Test 1: Fig. 4b1, c1). The peak values are as small as the minor peak for the observed SI-array CC (Fig. 4b, c). In the test, including a synthetic ISC signal with an adequate amplitude and ambient noise, the peak values of the synthetic array CCs are smaller than the observation, even if the peak values for the SI-array CC are similar to the observation (Test 2: Fig. 4b2, c2). A larger synthetic ISC signal could reproduce the observed peak values for the array CCs. However, it also produced an overly large ISC peak value in the synthetic SI-array CC (Test 3: Fig. 4b3, c3) and weakened the peak for the correlation response at -0.8 s. Adding non-acoustic noise to the synthetic SI microphone data could suppress the peak in the synthetic SI-array CC but erase the peak at -0.8 s (Test 4: Fig. 4b4, c4). The IWC fumarole signal is necessary to explain all

Table 2 Synthetic test parameters and the correlation peak values

	ISC amplitude (A_1)	IWC amplitude (A_2)	Noise amplitude in SI microphone $\left(A_{noise}^b\right)$	Peak value of array CC	Peak value of SI-array CC in $+$ 0.8 s	Peak value of SI-array CC in $-$ 0.8 s
Observation	–	–	–	0.90	0.13	0.01
Test 1	0	0	0	0.12	0.02	0.03
Test 2	8	0	0	0.30	0.13	0.01
Test 3	25	0	0	0.90	0.50	0.005
Test 4	25	0	0.4	0.90	0.13	None
Test 5	25	2	0.4	0.90	0.13	0.01

The noise amplitudes in Eq. 5 are fixed as $A_{noise}^n = 0 (n = $ A1, A2, A3), and $A_k = 1$

the peak values for the CCs (Test 5: Fig. 4b5, c5, Table 2), at least in these synthetic tests. From the above discussion, we concluded that the IWC fumarole signal formed the minor peak for the SI-array CC.

Power spectrum

At the array, the contribution of the ISC fumarole is significant (Table 1). Thus, the power spectrum of the array elements (green line in Fig. 3e) should have been characterized by the infrasound signal from the ISC fumarole. The distinctive feature is the power concentration around 10 Hz and 35 Hz, which was seen throughout the observation period (Fig. 2c). Although the significant power at $\sim$ 35 Hz is found in both power spectra for the IWC (the red line in Fig. 3e1) and ISC signals (the blue line in Fig. 3e2), the numerical tests using synthetic waveforms confirm it to originate from the ISC signal (Additional file 1: S7).

Identification of the mechanism generating the power at $\sim$ 10 Hz or $\sim$ 35 Hz would be important for investigating the fumarole. In volcanoes, harmonic monochromatic sources are often observed and modeled (e.g., Fee et al. 2010; Ripepe et al. 2010; Goto et al. 2011; Yokoo et al. 2019). Subsurface topographical resonances, such as the Helmholtz resonance (Fee et al. 2010; Goto et al. 2011; Vergniolle and Caplan-Auerbach 2004) or the resonance of the conduit (Watson et al. 2019), have been considered. Similarly, resonance frequencies of the fumarolic vent system under the ground might enhance the power at $\sim$ 10 Hz or $\sim$ 35 Hz. The ground topography also significantly affects the power spectral shape (Yamakawa 2022). There is a small wall behind the ISC fumarole (Fig. 2c), which might have influenced the resonance frequency of the fumarolic vent system above ground. Further investigation is needed to understand the fumarolic infrasound characterization mechanisms.

VSA array and SI microphone

Our methods and results should improve the future infrasonic observation in regions where a dominant source and minor sources coexist, such as a multi-edifice volcano. We have confirmed that both the SI microphone close to the source and the VSA array play essential roles in evaluating the IWC fumarole.

The SI-array CC reveals the contribution of the IWC fumarole, even though the array CC alone fails to identify it due to the poor SN ratio ($\sim 10^{-3}$, as in Table 1). Alternatively, if we use the SI microphone with another single microphone instead of the VSA array, we have only the single pair of the SI-array CC. Then, one might doubt that the weak correlation peak as small as 0.01 is a signal. The SI-array CCs allow us not only to confirm the signal but also to resolve the source regions. Also, this study points out a fundamental problem with two-station CCs: they may exhibit a false signal due to the correlation response of ambient noise.

Summary

Identifying each source's contribution is a challenging but demanded task in monitoring multiple infrasound sources. We undertook this task by combining a three-microphone VSA array with a single microphone at Kirishima Iwo-Yama, where two active fumaroles (ISC and IWC) emanated persistent infrasonic signals. Two kinds of microphones (a condenser microphone and a newly developed power-saving MEMS microphone) were used to confirm the microphone performance enough to be used in a VSA array. The VSA array at 150 m away from the ISC fumarole and 300 m from the IWC fumarole estimated the significant contribution of the ISC that was more powerful than the IWC. All methods, including the lag-time analysis, MUSIC algorithm, and CLEAN beamforming, identified signals from the ISC,

Yamakawa *et al. Earth, Planets and Space*   (2023) 75:26

Page 11 of 12

but none resolved the IWC fumarole. However, combining the VSA array with the SI microphone installed near the IWC fumarole successfully distinguished the two sources. Then, we estimated the individual source amplitudes and spectra with some approximations (monopole sources and homogeneous propagation). We also pointed out that the two-station cross-correlation analysis could exhibit false sources due to ambient noise and demonstrated that the VSA array could solve the problem. The microphones, array deployment, and analysis methods presented in this paper will be useful for resolving weak multiple infrasonic sources and monitoring the fumarolic activity of volcanoes.

Supplementary Information

The online version contains supplementary material available at https://doi.org/10.1186/s40623-023-01777-9.

> **Additional file: S1.** Supporting materials.

Author contributions
KY developed the methods, performed the analyses, and drafted the manuscript, supported by MI. KY, MI, DM, and TM conducted the field experiment, and HT and RW developed the MEMS infrasound sensors. All authors read and approved the final manuscript. IS led the project to develop the MEMS infrasound sensor. All authors read and approved the final manuscript.

Availability of data and materials
The data sets used and/or analyzed during the current study are available from the corresponding author on reasonable request.

Declarations

Competing interests
The authors declare that they have no competing interests.

Author details
[1]Mount Fuji Research Institute Yamanashi Prefectural Government, 5597-1 Kenmarubi, Kamiyoshida, Fujiyoshida, Yamanashi 403-0005, Japan. [2]Earthquake Research Institute, University of Tokyo, Tokyo 113-0032, Japan. [3]Institute of Seismology and Volcanology, Faculty of Science, Kyushu University, Shimabara 855-0843, Japan. [4]Department of Mechanical Engineering, Faculty of Science and Technology, Keio University, 3-14-1 Hiyoshi, Kouhoku-ku, Yokohama-City, Kanagawa 223-8522, Japan. [5]Department of Intelligent Robotics, Toyama Prefectural University, Toyama 939-0398, Japan.

References
Aiuppa A, Federico C, Giudice G, Gurrieri S (2005) Chemical mapping of a fumarolic field: la Fossa crater, Vulcano Island (Aeolian Islands, Italy). Geophys Res Lett. https://doi.org/10.1029/2005GL023207

Bensen GD, Ritzwoller MH, Barmin MP, Levshin AL, Lin F, Moschetti MP, Shapiro NM, Yang Y (2007) Processing seismic ambient noise data to obtain reliable broad-band surface wave dispersion measurements. Geophys J Int 169(3):1239–1260. https://doi.org/10.1111/j.1365-246X.2007.03374.x

Brenguier F, Shapiro N, Campillo M, Ferrazzini V, Duputel Z, Coutant O, Nercessian A (2008) Towards forecasting volcanic eruptions using seismic noise. Nat Geosci 1:126–130. https://doi.org/10.1038/ngeo104

Cannata A, Hellweg M, Di Grazia G, Ford S, Alparone S, Gresta S, Montalto P, Patanè D (2009) Long period and very long period events at Mt. Etna volcano: Characteristics, variability and causality, and implications for their sources. J Volcanol Geoth Res 187(3–4):227–249. https://doi.org/10.1016/j.jvolgeores.2009.09.007

Chouet B, Saccorotti G, Martini M, Dawson P, De Luca G, Milana G, Scarpa R (1997) Source and path effects in the wave fields of tremor and explosions at Stromboli Volcano, Italy. J Geophys Res Solid Earth 102(B7):15129–15150. https://doi.org/10.1029/97JB00953

den Ouden OFC, Assink JD, Smets PSM, Shanni-Kadmiel S, Averbuch G, Evers LG (2020) CLEAN beamforming for the enhanced detection of multiple infrasonic sources. Geophys J Int 221:305–317. https://doi.org/10.1093/gji/ggaa010

Fee D, Garcés M, Patrick M, Chouet B, Dawson P, Swanson D (2010) Infrasonic harmonic tremor and degassing bursts from Halema'uma'u Crater, Kilauea Volcano, Hawaii. J Geophys Res Solid Earth. https://doi.org/10.1029/2010JB007642

Fee D, Garces M, Orr T, Poland M (2011) Infrasound from the 2007 fissure eruptions of Kīlauea Volcano, Hawai'i. Geophys Res Lett. https://doi.org/10.1029/2010GL046422

Fischer TP (2008) Fluxes of volatiles (H_2O, CO_2, N_2, Cl, F) from arc volcanoes. Geochem J 42(1):21–38. https://doi.org/10.2343/geochemj.42.21

Goto A, Johnson JB (2011) Monotonic infrasound and helmholtz resonance at Volcan Villarrica (Chile). Geophys Res Lett. https://doi.org/10.1029/2011GL046858

Haney MM (2009) Infrasonic ambient noise interferometry from correlations of microbaroms. Geophys Res Lett. https://doi.org/10.1029/2009GL040179

Hirose T, Nakahara H, Nishimura T (2017) Combined use of repeated active shots and ambient noise to detect temporal changes in seismic velocity: application to Sakurajima volcano, Japan. Earth Planets Space 69:42. https://doi.org/10.1186/s40623-017-0613-7

Iezzi AM, Matoza RS, Fee D, Kim K, Jolly AD (2022) Synthetic evaluation of infrasonic multipole waveform inversion. J Geophys Res Solid Earth 127(1):e2021JB023223. https://doi.org/10.1029/2021JB023223

Iguchi M (2013) Magma movement from the deep to shallow Sakurajima Volcano as revealed by geophysical observations (<Special Section> Sakurajima Special Issue). Bull Vol Soc Jpn 58(1):1–18. https://doi.org/10.18940/kazan.58.1_1

Ikeda W, Ichihara M, Honda R, Aoyama H, Takahashi H, Yoshimoto M, Sakai S (2022) Experiment of infrasound monitoring for snow avalanche at My. Fuji Seppyo 84(5):421–432. https://doi.org/10.5331/seppyo.84.5_421

Johnson JB, Palma JL (2015) Lahar infrasound associated with Volcán Villarrica's 3 March 2015 eruption. Geophys Res Lett 42(15):6324–6331. https://doi.org/10.1002/2015GL065024

Marchetti E, Ripepe M, Ulivieri G, Caffo S, Privitera E (2009) Infrasonic evidences for branched conduit dynamics at Mt. Etna volcano, Italy. Geophys Res Lett. https://doi.org/10.1029/2009GL040070

McKee K, Fee D, Yokoo A, Matoza RS, Kim K (2017) Analysis of gas jetting and fumarole acoustics at Aso Volcano, Japan. J Volcanol Geoth Res. https://doi.org/10.1016/j.jvolgeores.2017.03.029

Minh-Dung N, Takahashi H, Uchiyama T, Matsumoto K, Shimoyama I (2013) A barometric pressure sensor based on the air-gap scale effect in a cantilever. Appl Phys Lett 103(14):143505. https://doi.org/10.1063/1.4824027

Muramatsu D, Matsushima T, Ichihara M (2021) Reconstructing surface eruptive sequence of 2018 small phreatic eruption of Iwo-yama volcano, Kirishima Volcanic Complex, Japan, by infrasound cross-correlation analysis. Earth Planets Space 73(1):1–10. https://doi.org/10.1186/s40623-020-01344-6

Muramatsu D, Ichihara M, Matsushima T, Kuwano O, Tajima Y (2022) Surface eruptive dynamics of 2018 small phreatic eruption of Iwo-Yama volcano,

Japan: constraints from seismo-acoustic observation and mud suspension rheology. J Volcanol Geoth Res 421:107452. https://doi.org/10.1016/j.jvolgeores.2021.107452

Nishida K, Mizutani Y, Ichihara M, Aoki Y (2020) Time-lapse monitoring of seismic velocity associated with 2011 Shinmoe-dake eruption using seismic interferometry: an extended Kalman filter approach. J Geophys Res Solid Earth 125(9):e2020JB020180. https://doi.org/10.1029/2020JB020180

Ortiz HD, Matoza RS, Johnson JB, Hernandez S, Anzieta JC, Ruiz MC (2021) Autocorrelation infrasound interferometry. J Geophys Res Solid Earth 126(4):e2020JB020513. https://doi.org/10.1029/2020JB020513

Ripepe M, Marchetti E (2002) Array tracking of infrasonic sources at Stromboli volcano. Geophys Res Lett 29(22):33–41. https://doi.org/10.1029/2002GL015452

Ripepe M, Marchetti E, Bonadonna C, Harris AJ, Pioli L, Ulivieri G (2010) Monochromatic infrasonic tremor driven by persistent degassing and convection at Villarrica Volcano, Chile. Geophys Res Lett. https://doi.org/10.1029/2010GL043516

Salvatore V, Silleni A, Corneli D, Taddeucci J, Palladino DM, Sottili G, Bernini D, Andronico D, Cristaldi A (2018) Parameterizing multi-vent activity at Stromboli Volcano (Aeolian Islands, Italy). Bull Volcanol 80(7):1–17. https://doi.org/10.1007/s00445-018-1239-8

Schmidt R (1986) Multiple emitter location and signal parameter estimation. IEEE Trans Antennas Propag 34:276–280. https://doi.org/10.1109/TAP.1986.1143830

Shapiro NM, Campillo M (2004) Emergence of broadband Rayleigh waves from correlations of the ambient seismic noise. Geophys Res Lett. https://doi.org/10.1029/2004GL019491

Shields DF (2005) Low-frequency wind noise correlation in microphone arrays. J Acoust Soc Am 117(6):3489–3496. https://doi.org/10.1121/1.1879252

Tajima Y, Nakada S, Maeno F, Huruzono T, Takahashi M, Inamura A, Matsushima T, Nagai M, Funasaki J (2020) Shallow magmatic hydrothermal eruption in April 2018 on Ebinokogen Ioyama volcano in Kirishima volcano group, Kyushu, Japan. Geosciences 10(5):183. https://doi.org/10.3390/geosciences10050183

Takahashi H, Suzuki A, Iwase E, Matsumoto K, Shimoyama I (2012) MEMS microphone with a micro Helmholtz resonator. J Micromech Microeng 22:085019

Tam C, Viswanathan K, Ahuja KK, Panda J (2008) The sources of jet noise: experimental evidence. J Fluid Mech 615:253–292. https://doi.org/10.1017/S0022112008003704

Tonegawa T, Nishida K, Watanabe T, Shiomi K (2009) Seismic interferometry of teleseicmic S-wave coda for retrieval of body waves: an application to the Philippine Sea slab underneath the Japanese Islands. Geophys J Int 178(3):1574–1586. https://doi.org/10.1111/j.1365-246X.2009.04249.x

Vergniolle S, Caplan-Auerbach J (2004) Acoustic measurements of the 1999 basaltic eruption of Shishaldin volcano, Alaska—2. Precursor to the Subplinian phase. J Volcanol Geoth Res 137:135–151. https://doi.org/10.1016/j.jvolgeores.2004.05.004

Wada R, Takahashi H (2020) Time response characteristics of a highly sensitive barometric pressure change sensor based on MEMS piezoresistive cantilevers. Jpn J Appl Phys 59(7):070906

Wallace PJ (2005) Volatiles in subduction zone magmas: concentrations and fluxes based on melt inclusion and volcanic gas data. J Volcanol Geoth Res 140(1–3):217–240. https://doi.org/10.1016/j.jvolgeores.2004.07.023

Wapenaar K, van del Neut J, Ruigrok E, Draganov D, Hunziker J, Slob E, Thorbecke J, Snieder R (2011) Seismic interferometry by crosscorrelation and by multidimensional deconvolution: a systematic comparison. Geophys J Int 185(3):1335–1364. https://doi.org/10.1111/j.1365-246X.2011.05007.x

Watson LM, Dunham EM, Johnson JB (2019) Simulation and inversion of harmonic infrasound from open-vent volcanoes using an efficient quasi-1D crater model. J Volcanol Geoth Res 380:64–79. https://doi.org/10.1016/j.jvolgeores.2019.05.007

Woulff G, McGetchin TR (1976) Acoustic noise from volcanoes: theory and experiment. Geophys J Int 45(3):601–616. https://doi.org/10.1111/j.1365-246X.1976.tb06913.x

Yamakawa K, Ichihara M, Ishii K, Aoyama H, Nishimura T, Ripepe M (2018) Azimuth estimations from a small aperture infrasonic array: test observations at Stromboli Volcano, Italy. Geophys Res Lett 45(17):8931–8938. https://doi.org/10.1029/2018GL078851

Yamakawa K, Ichihara M, Lacanna G, Sánchez C, Ripepe M (2022) Very-small-aperture 3-D infrasonic array for volcanic jet observation at Stromboli

Volcano. Geophys J Int 229(1):459–471. https://doi.org/10.1093/gji/ggab487

Yamakawa K (2022) Evaluation and practice of very-small-aperture infrasonic array for volcano monitoring. Dissertation, University of Tokyo

Yokoo A, Suzuki Y, Iguchi M (2014) Dual infrasound sources from a vulcanian eruption of Sakurajima volcano inferred from cross-array observation. Seismol Res Lett 85(6):1212–1222. https://doi.org/10.1785/0220140047

Yokoo A, Ishii K, Ohkura T, Kim K (2019) Monochromatic infrasound waves observed during the 2014–2015 eruption of Aso volcano, Japan. Earth Planets Space 71(1):1–14. https://doi.org/10.1186/s40623-019-0993-y

Publisher's Note